

# Role of the radiative stage for cosmic ray acceleration in SNRs

V. N. Zirakashvili,\* and V. S. Ptuskin,

*Pushkov Institute of Terrestrial Magnetism, Ionosphere and Radiowave Propagation, 108840, Troitsk, Moscow, Russia*

Accepted 2021 December 15. Received 2021 December 12; in original form 2021 November 20

## ABSTRACT

We consider diffusive shock acceleration in supernova remnants throughout their evolution including a radiative stage. It is found that a more efficient acceleration and fast exit of particles at the radiative stage results in the hardening of the source cosmic ray proton and electron spectra at energies  $\sim 100 - 500$  GeV. The effect is stronger for cosmic ray electrons.

**Key words:** cosmic rays – acceleration of particles – supernova remnants

## 1 INTRODUCTION

Supernova remnants (SNRs) are considered now as a principle source of Galactic cosmic rays (CRs). It is believed that the diffusive shock acceleration (DSA) mechanism (Krymsky 1977; Bell 1978; Axford et al. 1977; Blandford & Ostriker 1978) operates in the vicinity of shocks in SNRs. During the last decades, the modern X-ray and gamma-ray observations supplied the evidence of the presence of multi-TeV energetic particles in these astrophysical objects (see e.g. Lemoine-Goumard (2014) for a review).

Usually the existing DSA models are applied for young SNRs where the most energetic CRs are accelerated. However, lower energy particles are produced in older SNRs either. The investigation of CR acceleration in SNRs throughout all evolutionary stages is important for the calculation of overall CR spectra produced by SNRs.

In this paper, we describe the modifications of our non-linear DSA model (Zirakashvili & Ptuskin 2012) designed for investigation of DSA over the entire life of SNRs. The preliminary results on the application of this modified model to gamma ray bright SNRs W28, W44, and IC443 were reported in Zirakashvili (2018); Zirakashvili & Ptuskin (2016a, 2018a). The main new features are the gas ionization by the radiation of the remnant, radiative cooling of the gas, and damping of MHD waves on neutral atoms at the late stages of SNR evolution. We also performed the modeling of acceleration and production of broad-band electromagnetic emission in the young SNR Tycho and middle-aged SNR W44 to adjust the parameters of the model.

The paper is organized as follows. In the next Section 2, we describe our model. CR acceleration in IIP type SNRs evolving in the dense medium and modeling of nonthermal emission of SNR W44 is presented in Section 3. The modeling of Ia Type SNRs evolving in a more rarefied medium and the modeling of SNR Tycho are described in Section 4. The discussion of results and conclusions are given in Sections 5 and 6.

## 2 NONLINEAR DIFFUSIVE SHOCK ACCELERATION MODEL

Details of our basic model of nonlinear DSA can be found in Zirakashvili & Ptuskin (2012). The model contains coupled spherically symmetric hydrodynamic equations and the transport equations for energetic protons, ions, and electrons. The forward and reverse shocks are included in the consideration.

Damping of magnetohydrodynamic (MHD) waves due to the presence of neutral atoms is important for SNRs expanding in not fully ionized gas. To take this effect into account we add the equation that describes the transport and generation of MHD waves (see Eq.(5) below).

The hydrodynamical equations for the gas density  $\rho(r,t)$ , gas velocity  $u(r,t)$ , gas pressure  $P_g(r,t)$ , wave pressure  $P_w(r,t)$ , pressure of the regular magnetic field  $P_m(r,t)$ , and the equation for isotropic part of the cosmic ray proton momentum distribution  $N(r,t,p)$  in the spherically symmetrical case are given by

$$\frac{\partial \rho}{\partial t} = -\frac{1}{r^2} \frac{\partial}{\partial r} r^2 u \rho \quad (1)$$

$$\frac{\partial u}{\partial t} = -u \frac{\partial u}{\partial r} - \frac{1}{\rho} \left( \frac{\partial P_g}{\partial r} + \frac{\partial P_c}{\partial r} + \frac{\partial P_w}{\partial r} + \frac{\partial P_m}{\partial r} \right) \quad (2)$$

$$\frac{1}{\gamma_g - 1} \left( \frac{\partial P_g}{\partial t} + u \frac{\partial P_g}{\partial r} + \frac{\gamma_g P_g}{r^2} \frac{\partial r^2 u}{\partial r} \right) = -\Lambda(T_e) n^2 + H_c + 2\Gamma_n \frac{P_w}{\gamma_w - 1} - \xi_A V_{Ar} (1 - h_w) \frac{\partial P_c}{\partial r} \quad (3)$$

$$\frac{\partial P_m}{\partial t} + u \frac{\partial P_m}{\partial r} + \frac{\gamma_m P_m}{r^2} \frac{\partial r^2 u}{\partial r} = 0 \quad (4)$$

$$\frac{\partial P_w}{\partial t} + (u + \xi_A V_{Ar}) \frac{\partial P_w}{\partial r} + \frac{P_w}{r^2} \frac{\partial r^2 (\gamma_w u + \xi_A V_{Ar})}{\partial r} = -h_w (\gamma_w - 1) \xi_A V_{Ar} \frac{\partial P_c}{\partial r} - 2\Gamma_n P_w \quad (5)$$

\* E-mail: zirak@izmiran.ru

$$\begin{aligned}
\frac{\partial N}{\partial t} &= \frac{1}{r^2} \frac{\partial}{\partial r} r^2 D(p, r, t) \frac{\partial N}{\partial r} - w \frac{\partial N}{\partial r} + \frac{\partial N}{\partial p} \frac{p}{3r^2} \frac{\partial r^2 w}{\partial r} \\
&+ \frac{1}{p^2} \frac{\partial}{\partial p} p^2 b(p) N + \\
&\frac{\eta_f X_i \delta(p - p_f)}{4\pi p_f^2 m} \rho(R_f + 0, t) (\dot{R}_f - u(R_f + 0, t)) \delta(r - R_f(t)) \\
&+ \frac{\eta_b \delta(p - p_b)}{4\pi p_b^2 m} \rho(R_b - 0, t) (u(R_b - 0, t) - \dot{R}_b) \delta(r - R_b(t)) \quad (6)
\end{aligned}$$

Here  $P_c = 4\pi \int dp p^3 v N / 3$  is the cosmic ray pressure,  $w(r, t)$  is the advection velocity of cosmic rays,  $T_e$ ,  $\gamma_g$  and  $n$  are the gas temperature, adiabatic index, and number density respectively,  $\gamma_w$  is the wave adiabatic index,  $D(r, t, p)$  is the cosmic ray diffusion coefficient. The radiative cooling of gas is described by the cooling function  $\Lambda(T_e)$ . The function  $b(p)$  describes the energy losses of particles. In particular, the Coulomb losses of sub-GeV ions and the radiative cooling are important in old SNRs. The energy of sub GeV ions goes to the gas heating described by the term  $H_c$  in Eq. (3).

Cosmic ray diffusion is determined by the scattering on magnetic inhomogeneities. The cosmic ray streaming instability increases the level of MHD turbulence in the shock vicinity (Bell 1978) and even significantly amplifies the absolute value of the magnetic field in young SNRs (Bell 2004; Zirakashvili & Ptuskin 2008a). It decreases the diffusion coefficient and increases the maximum energy of accelerated particles. The results of continuing theoretical study of this effect can be found in review papers (Bell 2014; Caprioli 2014).

Cosmic ray particles are scattered by moving waves and it is why the cosmic ray advection velocity  $w$  may differ from the gas velocity  $u$  by the value of the radial component of the Alfvén velocity  $V_{Ar} = V_A / \sqrt{3}$  calculated in the isotropic random magnetic field:  $w = u + \xi_A V_{Ar}$ . The factor  $\xi_A$  describes the possible deviation of the cosmic ray drift velocity from the gas velocity. We use values  $\xi_A = 1$  and  $\xi_A = -1$  upstream of the forward and reverse shocks respectively, where Alfvén waves are generated by the cosmic ray streaming instability and propagate in the corresponding directions.

The situation is less clear in the downstream region of the shocks. Usually, the Alfvén drift is not considered here. However, it is known that Alfvén transport in the downstream region suggested at phenomenological level (Zirakashvili & Ptuskin 2008b) results in steeper spectra of accelerated particles. This also allows avoiding a cosmic ray overproduction in evolutionary models of SNRs (Ptuskin et al. 2010).

Recently the Alfvén transport in the downstream region was indeed observed in hybrid modeling of collisionless shocks (Haggerty & Caprioli 2020). It looks like some nonlinear magnetic structures are generated in the shock transition and move with Alfvén speed in the downstream region. The origin of these nonlinear waves is unclear. They can be large scale transverse Alfvén-like waves propagating in the isotropic tangled magnetic field with phase speed  $V_A / \sqrt{3}$  (Moffatt 1986). Or they somehow can be related to sonic waves generated at the shock front.

Below we take the Alfvénic transport in the downstream region into account. We use values  $\xi_A = -1$  and  $\xi_A = 1$  just downstream of forward and reverse shocks respectively. The Alfvénic transport takes place in the narrow region of thickness 0.1 of the distance between the shock and the contact discontinuity.

The pressure of generated waves  $P_w$  determines the scattering and

diffusion of energetic particles with charge  $q$ , momentum  $p$ , and speed  $v$

$$D = D_B \frac{P_m + P_w}{P_w}, \quad D_B = \frac{c p v}{3 q B}, \quad B = \sqrt{8\pi(P_m + P_w)} \quad (7)$$

where  $B$  is the total magnetic field strength, while  $P_m$  is the pressure of the regular field. At high wave amplitudes, the diffusion coefficient coincides with the Bohm diffusion coefficient  $D_B$ .

The parameter  $h_w$  in Eqs. (3,5) describes the fraction of the wave energy produced by the streaming instability. We use the following dependence  $h_w(P_w/P_m)$

$$h_w = 1, \quad \frac{P_w}{P_m} < 10; \quad h_w = 0.7, \quad \frac{P_w}{P_m} > 10. \quad (8)$$

At high amplitudes, the waves are damped and the fraction  $1 - h_w$  of energy goes into the gas heating upstream of the shocks (McKenzie & Völk 1982) that is described by the last term in Eq. (3). The heating and wave generation limits the total compression ratio of cosmic ray modified shocks. The value of  $h_w$  regulates the magnetic amplification in the upstream region of the shock. Since the amplified field is transported into the downstream region,  $h_w$  also determines the efficiency of the Alfvénic transport in this region and regulates the spectral slope of accelerated particles. Its value  $h_w = 0.7$  was adjusted to reproduce broad-band modeling of Tycho SNR (see Section 4 below).

The low seed level of the interstellar turbulence  $P_w = 10^{-6} B_0^2 / 8\pi$  is prescribed at the simulation boundary at  $r = 2R_f$ . Since the flux of escaped highest energy particles amplifies waves exponentially in time the results depend only logarithmically on the seed level.

In the shock transition region the wave pressure is increased by a factor of  $\sigma^{\gamma_w}$ , where  $\sigma$  is the shock compression ratio. Its impact on the shock dynamics is taken into account via the Hugoniot conditions.

Below we use the adiabatic index of Alfvén waves  $\gamma_w = 3/2$ . For this value of the adiabatic index, the wave pressure  $P_w = (\delta B)^2 / 8\pi$  equals the wave magnetic energy density. The pressure of the regular field  $P_m$  plays a dynamical role at the radiative phase when the field is strongly compressed in the downstream region and produces a significant anisotropic force in the radial direction. To take this into account we use the adiabatic index  $\gamma_m = 2$  for the regular magnetic field.

The rate of the neutral damping  $\Gamma_n = 0.5 v_{in}$  is determined by the frequency of ion neutral collisions  $v_{in}$  in the limit of the high wave frequencies  $\omega \gg v_{in}$ . The frequency of ion-neutral collisions is determined by charge-exchange process and is given by (Drury et al. 1996))

$$v_{in} = 8.9 \cdot 10^{-9} n_n \left( \frac{T}{10^4 \text{ K}} \right)^{0.4} \text{ s}^{-1}. \quad (9)$$

Here the number density  $n_n = X_n n_H$  of neutral hydrogen atoms is determined by the neutral fraction  $X_n$ . A useful review of DSA in partially ionized plasma can be found in Bykov et al. (2013).

The neutral fraction of hydrogen ions  $X_n$  is determined by equation

$$\frac{\partial X_n}{\partial t} = -u \frac{\partial X_n}{\partial r} + \alpha_{\text{rec}} n_H X_i^2 - X_n (q_{\text{th}} + q_{\text{ph}}) \quad (10)$$

where  $X_i = 1 - X_n$  is the fraction of ionized Hydrogen,  $\alpha_{\text{rec}}$  is the

recombination rate and  $q_{\text{th}}$  and  $q_{\text{ph}}$  are thermal ionization and photoionization rates respectively. The photoionization rate is given by

$$q_{\text{ph}}(r) = 2\pi \int_0^\pi \sin(\theta) d\theta \sigma_{\text{ph}} I(r, \theta) \quad (11)$$

Here  $\theta$  is the angle between the photon wavevector and radial direction and  $\sigma_{\text{ph}}$  is the photoionization cross-section of Hydrogen. The intensity of ionizing photons  $I(r, \theta)$  is determined from the equation of radiative transport

$$\cos(\theta) \frac{\partial I}{\partial r} - \frac{\sin(\theta)}{r} \frac{\partial I}{\partial \theta} = \frac{\Lambda_i(T_e) n^2}{4\pi I_H} - \sigma_{\text{ph}} I \quad (12)$$

and  $I_H = 13.6$  eV is the ionization potential of Hydrogen. The first term on the right-hand side is the emissivity of ionizing photons that was determined by the partial cooling function  $\Lambda_i(T)$  in the radiation range 300-910 angstrom of Landini & Fossi (1990).

Two last terms in Eq. (6) correspond to the injection of thermal protons with momenta  $p = p_f$ ,  $p = p_b$  and mass  $m$  at the forward and reverse shocks located at  $r = R_f(t)$  and  $r = R_b(t)$  respectively. The dimensionless parameters  $\eta_f$  and  $\eta_b$  determine the efficiency of injection.

The injection efficiency is taken to be independent of time  $\eta_f = 0.001$ , and the particle injection momentum is  $p_f = 2m(\dot{R}_f - u(R_f + 0, t))$ . Protons of mass  $m$  are injected at the forward shock and ions of mass  $M$  and mass to charge ratio  $A/Z = 2$  and injection efficiency  $\eta_b = 0.001$  are injected at the reverse shock.

For high Mach number shocks this injection efficiency and Alfvén transport in the downstream region limit the pressure of accelerated particles and the magnetic energy density at the level 10 – 20 % and 1.5 % of the ram pressure of the shock respectively. These numbers are comparable with ones observable in the hybrid modeling of collisionless shocks (Caprioli et al. 2020).

We neglect the pressure of energetic electrons and treat them as test particles. The evolution of the electron distribution is described by the equation analogous to Eq. (6) with function  $b(p)$  describing Coulomb, synchrotron, and inverse Compton (IC) losses and additional terms describing the production of secondary leptons by energetic protons and nuclei. The electron injection efficiency  $\eta_e$  at the forward shock was taken in the form

$$\eta_e = 7 \cdot 10^{-8} \left( \frac{V_f}{c} \right)^{-0.6} \quad (13)$$

where the numeric parameters were adjusted to reproduce the intensity of radio-emission in supernova remnants W44 and Tycho. This dependence of  $\eta_e$  on the shock velocity  $V_f$  results in a higher electron to proton ratio in older SNRs in comparison with the one in the young SNRs.

### 3 MODELING OF DIFFUSIVE SHOCK ACCELERATION IN SNR OF IIP SUPERNOVA

A significant part of core-collapse supernova explosion occurs in molecular gas. The stars with initial masses below  $12 M_\odot$  have no power stellar winds and therefore do not produce a strong modification of their circumstellar medium. The molecular cloud has been totally destroyed by stellar winds and supernova explosions of more massive stars at the instant of explosion. As a result, the star explodes in the inter-clump medium with the density  $5 - 25 \text{ cm}^{-3}$  (Chevalier 1999). Many such SNRs are observed in gamma rays now.

It is believed that the circumstellar medium is almost fully ionized by ultraviolet radiation from the remnant interior at the radiative

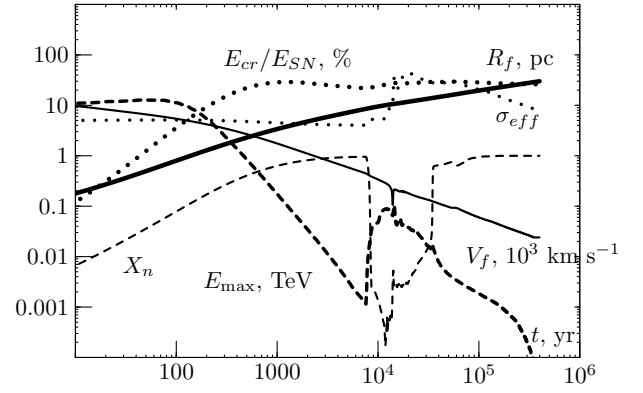


**Figure 1.** Dependence on time of the forward shock radius  $R_f$  (thick solid line), the shock speed  $V_f$  (thin solid line), the shock effective compression ratio  $\sigma_{\text{eff}}$  (thin dotted line), the maximum energy of particles accelerated at forward shock  $E_{\text{max}}$  (dashed line), the fraction of explosion energy transformed into cosmic rays  $E_{\text{cr}}/E_{\text{SN}}$  (thick dotted line) and neutral fraction  $X_n$  (thin dashed line) calculated for SNR of IIP supernovae.

stage (Chevalier 1999). The same is true for young SNRs because the gas is ionized by the radiation from the shock breakout and in the hot shock precursor produced by accelerated particles. Extended red super giant progenitors of IIP Type supernovae emit  $\sim 10^{48}$  erg of radiation during the shock breakout. This amount of energy is sufficient for the ionization of several dozens of solar masses of the circumstellar gas (Chevalier 2005). If so the shock propagates in the preionized medium at the free expansion phase and at the beginning of the Sedov stage. The amount of the breakout radiation is significantly smaller for compact progenitors of Ib/c and Ia type supernovae. However Wolf-Rayet progenitors itself ionize  $\sim 10^3 M_\odot$  of surrounding gas before the explosion. Some level of the preionization is also expected for Ia Type supernovae because of the ionizing radiation of the accreting white dwarf. In this regard the assumption of the full ionization is justified for almost all stages of the supernova remnant evolution. The only probable exception is the end of the Sedov stage when the shock might propagate in the neutral medium. In this picture, the number density of neutrals  $n_n$  is determined by the ionization history and by the recombination in ionized or preionized plasma.

Bright in GeV gamma-rays middle-aged SNR W44 at distance  $d = 2.8$  kpc from the Earth is at the radiative phase now and shows signs of interaction with molecular gas (Reach et al. 2005). It contains HI shell expanding with speed  $135 - 150 \text{ km s}^{-1}$  (Koo et al. 1995; Park et al. 2003).

The parameters of our supernova modeling are given in Table I. The explosion parameters were adjusted to reproduce broad-band observations of SNR W44. The explosion energy  $E_{\text{SN}}$  and ambient number density  $n_H$  were adjusted to reproduce the expansion speed of HI shell and the observable gamma-ray flux.

The numbers in the three last columns of Table I that is the age  $T$ , shock speed  $V_f$  and magnetic field strength  $B_f$  just downstream of the shock were obtained in the modeling.

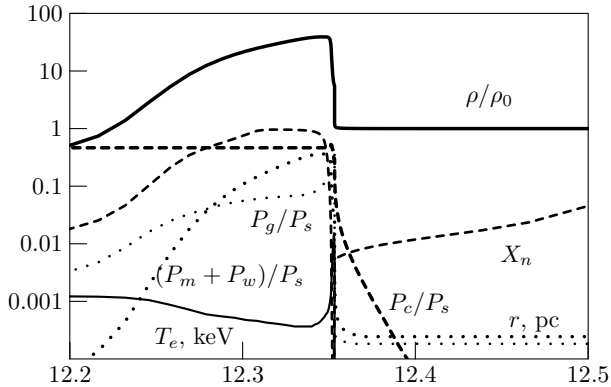
We use the parameter of ejecta velocity distribution  $k_{\text{SN}} = 9$  (this parameter describes the power-law density profile  $\rho_{ej} \propto r^{-k_{\text{SN}}}$  of the outer part of the ejecta that freely expands after supernova explosion).

The ionized fraction of Hydrogen  $X_i$  at the initial instant of time

[t]

**Table 1.** Physical parameters of SNRs modeled

Type	SNR	$d$	$R_f$	$E_{SN}$	$M_{ej}$	$k_{SN}$	$B_0$	$n_H$	$X_{i0}$	$R_i$	$T$	$V_f$	$B_f$
		kpc	pc	$10^{51}$ erg	$M_\odot$		$\mu$ G	$\text{cm}^{-3}$		pc	kyr	km/s	$\mu$ G
IIP	W44	2.8	12.35	1.8	10	9	5	7.0	0.01	4	23	160	51
Ia	Tycho	3.5	4.1	1.2	1.4	7	3	0.2	0.5	8	0.44	5300	210

**Figure 2.** Radial dependencies of the gas density (thick solid line), the gas temperature  $T_e$  (thin solid line), CR pressure (thick dashed line), neutral fraction  $X_n$  (dashed line), the magnetic energy density  $B^2/8\pi = P_m + P_w$  (dotted line), and the gas pressure  $P_g$  (thin dotted line) at  $T = 23$  kyr in the vicinity of the forward shock in SNR W44. The pressures are normalized to the ram pressure of the shock  $P_s = \rho_0 V_f^2$ 

was taken in the form

$$X_i = (1 - X_{i0}) \exp\left(-\left(\frac{r}{R_i}\right)^2\right) + X_{i0} \quad (14)$$

where the ionization fraction at infinity  $X_{i0}$  and the radius of the ionization zone  $R_i$  are given in Table I. It was assumed that about 40 solar masses of Hydrogen is ionized during the supernova explosion.

Figures (1)-(4) illustrate the results of our numerical calculations. The temporal evolution of the remnant and particle acceleration are illustrated in Fig.1. The maximum energy of particles  $E_{\max}$  at the forward shock was estimated as the energy where the function  $p^5 N(p)$  has a maximal value. The shock speed is almost constant at the initial free expansion stage. After one hundred years the Sedov stage begins. Maximum energy of particles is close to 20 TeV at this time. Later the maximum energy drops sharply because of the shock velocity decrease and because of the neutral damping of MHD waves. The neutral fraction  $X_n$  increases because of the recombination and later when the shock enters into a neutral medium. Strictly speaking the adequate description of DSA at this stage requires a kinetic treatment for the transport of neutral atoms near the shock (see [Morlino et al. \(2013\)](#)). We leave the detailed description of the acceleration at this stage to the future. It seems that this stage does not produce a strong impact on results because the injection rate is proportional to the ionized fraction  $X_i$  and therefore the production rate of cosmic rays at this phase is not high.

The ionizing radiation from the shock interior again ionizes the medium after 8 kyrs. At this instant of time, the boundary of the

ionization zone overtakes the forward shock. The acceleration efficiency increases because of higher injection rate.

Several thousands years after this the radiative stage begins when the cooling behind the shock results in the gas compression in this region and in the formation of a dense shell at the age  $T = 14$  kyrs. While the compression ratio of the shock is close to the standard value  $\sim 4$  the gas density continues to increase further downstream. To illustrate this we show in Fig.1 the effective compression ratio  $\sigma_{\text{eff}}$  that is the ratio of the maximum gas density behind the shock to the ambient gas density. This ratio increases up to the value of 40 that is limited by the presence of cosmic rays and regular magnetic fields. This gas compression results in a more efficient acceleration and in an enhanced flux of runaway highest energy particles. This, in turn, produces some temporary constant level of the maximum energy. In addition, the gas cooling behind the shock is accompanied by its recombination. The neutral gas of the shell absorbs the ionizing radiation from the hot remnant interior. This stops ionization in the far upstream region and gas ionized earlier begins to recombine. Particles accelerated earlier leave the neutral shell because of the damping of MHD waves. At 35 kyrs the shock reaches the boundary of the ionized region and enters the neutral medium. At later times the acceleration at the forward shock does not occur.

It should be noted that we use a simplified approach for the description of the radiative cooling and photoionization with the equilibrium cooling functions  $\Lambda(T_e)$  and  $\Lambda_i(T_e)$ . In reality, radiative cooling and photoionization depend on the ionization state of ions in plasma that is not in thermal equilibrium. However, we checked by performing a test run without cosmic rays that the reionization, the dense shell formation, and exit of the shock to the neutral medium occur at the same age as in the SNR modeling with a full application of the atomic physics ([Sarkar et al. 2021](#)).

Radial dependencies of physical quantities in SNR W44 at present ( $T = 23$  kyr) are shown in Fig.2. The gas temperature drops sharply downstream of the forward shock due to the radiative cooling and a thin neutral dense shell is formed behind the forward shock. We obtain the shell mass of the neutral Hydrogen  $640 M_\odot$  that is somewhat higher than the measured value of  $390 M_\odot$  ([Park et al. 2003](#)). The central part of the remnant is filled by the hot rarefied gas with a temperature of  $10^6 - 10^7$  K.

Results of multi-band modeling of SNR W44 are shown in Fig. 3. Thermal emission has two components. One is produced by the hot gas in the remnant interior while the lower energy component is produced by the dense gas that cooled and recombined behind the shock front. This gas produces a significant amount of the thermal radio emission that dominates the synchrotron radio emission at high frequencies.

The spectra of particles  $N_{int}$  produced during 400 kyr after supernova explosion are shown in Fig.4. They are calculated via the integration throughout the simulation domain and via the integration on time of the outward diffusive flux at the simulation boundary at

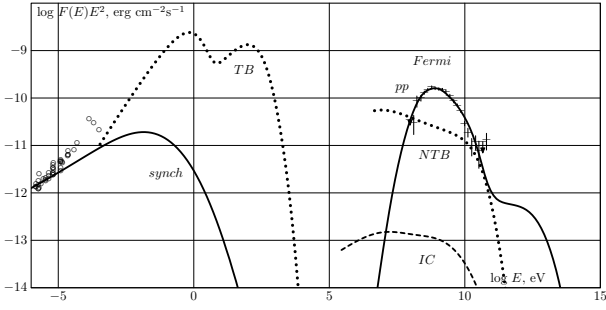


**Figure 3.** The results of modeling of electromagnetic radiation of W44. The following radiation processes are taken into account: synchrotron radiation of accelerated electrons (solid curve on the left), IC emission (dashed line), gamma-ray emission from pion decay (solid line on the right), thermal bremsstrahlung (dotted line on the left), nonthermal bremsstrahlung (dotted line on the right). Experimental data in gamma-rays by the Fermi LAT (Ackermann et al. 2013) (data with error bars) and in radio bands (Castelletti et al. 2007; Arnaud et al. 2016) (circles) are also shown.

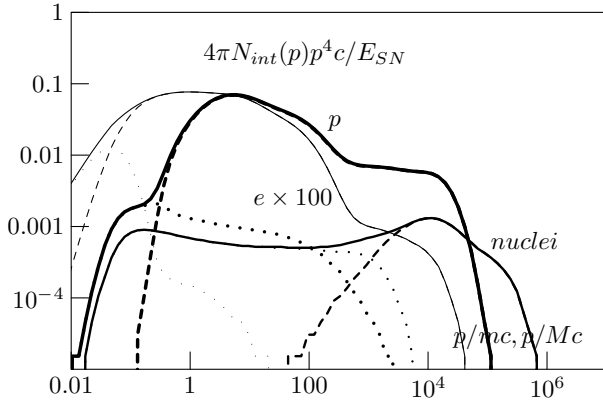


**Figure 4.** Spectra of protons (thick lines) and electrons (thin lines) produced at the forward shock, and nuclei (normal lines) produced at the reverse shock in SNR of Type IIP during 400 kyr after explosion. The spatially integrated spectra of particles (dotted lines), the spectra of particles escaped from the remnant (dashed lines), and the sum (solid lines) are shown.

$r = 2R_f$ . About 26% of the kinetic energy of the explosion is transferred to cosmic rays. Almost all this energy is gone with escaped particles. Note that almost all protons and electrons accelerated at the forward shock have left the remnant. This is because the neutral damping of MHD waves, which confine cosmic rays, was taken into account in the downstream region. In this regard, the proton and electron spectra shown in Fig.4 are the source spectra of galactic CRs. This is not so for the ion spectrum. A significant part of ions accelerated at the reverse shock are still confined in the central part of the remnant, where the gas is fully ionized. The exit of particles from the ionized regions of SNR is regulated by another kind of damping of MHD waves that is not considered here.

As was mentioned before the acceleration efficiency increases just before and after the transition to the radiative stage. The corresponding cosmic ray spectra of protons and electrons shows a spectral hardening at several hundreds GeV. The effect is stronger for electrons because their injection rate increases with time according to Eq. (13).

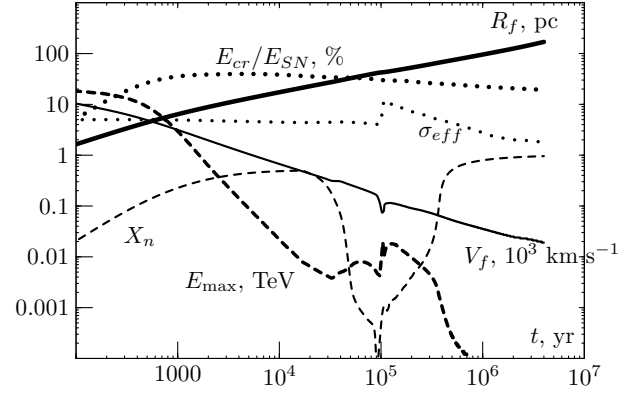


**Figure 5.** Dependence on time of the forward shock radius  $R_f$  (thick solid line), the shock speed  $V_f$  (thin solid line), the effective shock compression ratio  $\sigma_{eff}$  (thin dotted line), the maximum energy of particles accelerated at forward shock  $E_{max}$  (dashed line), the fraction of explosion energy transformed into cosmic rays  $E_{cr}/E_{SN}$  (thick dotted line) and neutral fraction  $X_n$  (thin dashed line) calculated for SNR of Ia supernovae.

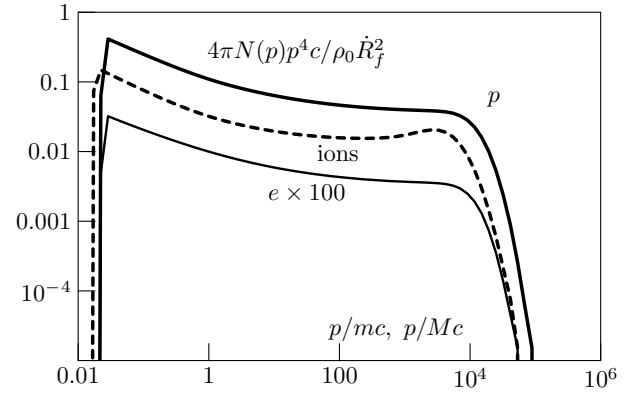


**Figure 6.** The spectra of particles in Tycho SNR. Proton and electron spectra at the forward shock and spectrum of ions accelerated at the reverse shock are shown.

#### 4 MODELING OF DSA IN SNR OF TYPE IA SUPERNOVA

The parameters of supernova modeling are given in Table I. The explosion parameters were adjusted to reproduce multiwave observations of young SNR Tycho. The distance to this SNR is very uncertain. So we fix the explosion energy to a value  $E_{SN} = 1.2 \cdot 10^{51}$  erg of the one-dimensional delayed detonation model of the Tycho supernova explosion (Badenes et al. 2006). Then the distance and the ambient number density  $n_H$  were adjusted to reproduce the age of SNR and its angular diameter of  $8'$ . The parameter  $h_w = 0.7$  in Eqs. (3),(5) and (8) was adjusted to reproduce the observable gamma-ray spectrum.

It was assumed that about 5 solar masses of Hydrogen is ionized before and during the supernova explosion.

The remnant evolves in a low-density medium. That is why the transition to the radiative stage occurs at 100 kyrs. The regular magnetic field produces a stronger limitation of  $\sigma_{eff} \sim 10$  at this stage.

Spectra of accelerated in Tycho SNR protons, ions, and electrons at present are shown in Fig.6. They are rather soft due to the Alfvénic transport in the downstream region. This also provides a good agreement with radio, X-ray, and gamma-ray data (see Fig.7).

The spectra of particles  $N_{int}$  produced during 4 Myr after super-

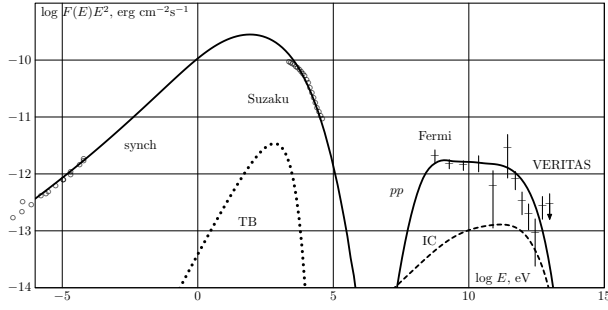


**Figure 7.** The results of modeling of electromagnetic radiation of Tycho SNR. The following radiation processes are taken into account: synchrotron radiation of accelerated electrons (solid curve on the left), IC emission (dashed line), gamma-ray emission from pion decay (solid line on the right), thermal bremsstrahlung (dotted line on the left). Experimental data in gamma-rays by the Fermi LAT and VERITAS (Archambault et al. 2017); (data with error bars), radio (Klein et al. 1979), and analytical approximation of continuum X-rays by Suzaku (Tamagawa et al. 2009) (circles) are also shown.

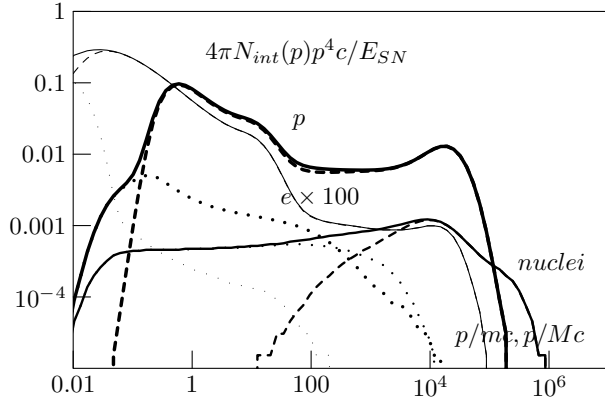


**Figure 8.** Spectra of protons (thick lines) and electrons (thin lines) produced at the forward shock, and nuclei (normal lines) produced at the reverse shock in SNR of Type Ia during 4 Myr after explosion. The spatially integrated spectra of particles (dotted lines), the spectra of particles escaped from the remnant (dashed lines), and the sum (solid lines) are shown.

nova explosion are shown in Fig.8. They are calculated via the integration throughout the simulation domain and via the integration on time of the outward diffusive flux at the simulation boundary at  $r = 2R_f$ . About 19% of the kinetic energy of the explosion is transferred to cosmic rays. Almost all this energy is gone with escaped particles. The maximum energy of escaped particles is 50 TeV for this SNR. Similar to the case of IIP type SNR almost all accelerated protons and electrons left the remnant and their spectra can be considered as source spectra of galactic cosmic rays.

The energy of the hardening is lower for Ia Type SNRs. Note that transition to the radiative stage occurs when the shock radius is 40 pc. Probably in many cases, the shock will collide with a denser medium before the transition. Then the situation will be similar to the one considered in the previous Section.

## 5 DISCUSSION

The transition to the radiative stage begins when the radiative losses are comparable with adiabatic losses in the downstream region (see

the corresponding terms in Eq. (3)). Assuming a linear profile of the gas velocity we get

$$\Lambda(T_e)n_H^2\sigma^2 \sim \frac{(\sigma-1)\gamma_g\xi_g\rho V_f^3}{(\gamma_g-1)\sigma R}. \quad (15)$$

Here  $\xi_g = P_g/\rho V_f^2$  is the ratio of the gas pressure just downstream of the shock  $P_g$  to the shock ram pressure  $\rho V_f^2$ ,  $\sigma$  is the shock compression ratio. Using the relation

$$\rho V_f^2 R_f^3 = 0.2E_{SN} \quad (16)$$

at the Sedov stage and numeric values  $\sigma = 4$ ,  $\gamma_g = 5/3$ , and  $\xi_g = 0.75$  we can obtain the shock speed  $V_{rad}$  at the time of transition

$$V_{rad} = 250 \text{ km s}^{-1} n_H^{2/11} \left( \frac{E_{SN}}{10^{51} \text{ erg}} \right)^{1/11} \left( \frac{\Lambda}{10^{-22} \text{ erg cm}^3 \text{ s}^{-1}} \right)^{3/11} \quad (17)$$

In the absence of damping the maximum energy  $E_{max}$  of accelerated particles can be found from the condition that the magnetic field amplified by the cosmic ray streaming instability has enough time to grow from the initial value of  $B_b$ , that is  $\Gamma_{cr}T = \ln(B/B_b) \sim 10$  during the age  $T$ .

In young SNRs the streaming instability is non-resonant while in older remnants it is resonant. In spite of the different nature the rates of the resonant and non-resonant instabilities are given by similar expressions. For the estimate we use the non-resonant instability rate  $\Gamma_{cr}$  (Bell 2004)

$$\Gamma_{cr} = \frac{J_{el}B}{2c\rho v_A}, \quad (18)$$

where  $J_{el}$  is the electric current of the highest energy cosmic rays escaping into the upstream region. This results in expression (Zirakashvili & Ptuskin 2008a)

$$E_{max} = \frac{\eta_{esc}qBV_f^3T}{4cv_A \ln(B/B_b)} = 2 \text{ TeV} \left( \frac{\eta_{esc}}{0.05} \right) \left( \frac{V_f}{10^3 \text{ km s}^{-1}} \right)^2 m_{exp} n_H^{0.5} R_{pc}. \quad (19)$$

Here  $\eta_{esc}$  is the ratio of the energy flux of highest energy particles to the shock energy flux  $\rho V_f^3/2$  and  $m_{exp} = V_f T/R_f$  is the expansion parameter of the shock. At the beginning of the Sedov stage  $V_f^2 = 2E_{SN}/M_{ej}$ ,  $R_f = (3M_{ej}/4\pi m \cdot 1.4n_H)^{1/3}$  and

$$E_{max} = 2 \left( \frac{3}{4\pi \cdot 1.4} \right)^{1/3} \frac{m_{exp}\eta_{esc}qBE_{SN}}{4m^{1/3}n_H^{1/3}M_{ej}^{2/3}cv_A \ln(B/B_b)} = 400 \text{ TeV} \left( \frac{\eta_{esc}}{0.05} \right) \left( \frac{E_{SN}}{10^{51} \text{ erg}} \right) \left( \frac{M_{ej}}{M_\odot} \right)^{-2/3} m_{exp} n_H^{1/6}. \quad (20)$$

The value  $\eta_{esc} = 0.05$  corresponds to the effectively accelerating shock with  $E^{-2}$  spectrum of particles and CR pressure of the order 50% of the shock ram pressure. The Alfvénic transport downstream results in steeper spectra, lower CR pressure (see Fig.6), and lower  $\eta_{esc} \sim 0.01$ . Then for parameters of IIP and Ia Type supernovae (see Table I) and  $m_{exp} = 0.5$  we get the maximum energies of 20 TeV and 30 TeV at the beginning of the Sedov stage in qualitative agreement with Fig.1 and Fig.5.

So the maximum energies determined by CR streaming instability are not higher than 100 TeV in SNRs considered. Higher energies can be reached for SNRs shocks propagating in rarefied bubbles created by Type Ib/c supernova progenitors where the medium is prepared for the efficient DSA (Zirakashvili & Ptuskin 2018b, 2021) or in dense progenitor winds of II Type SNRs (Zirakashvili & Ptuskin 2016b).

The maximum energy at the instant of transition to the radiative stage  $E_{\text{rad}}$  can be found from equations (16),(17), (19)

$$E_{\text{rad}} = 200 \text{ GeV} \left( \frac{\eta_{\text{esc}}}{0.01} \right) n_H^{9/22} \left( \frac{E_{\text{SN}}}{10^{51} \text{ erg}} \right)^{5/11} \left( \frac{\Lambda}{10^{-22} \text{ erg cm}^3 \text{ s}^{-1}} \right)^{4/11} \quad (21)$$

where the value  $m_{\text{exp}} = 0.4$  was used. This gives the energy of hardening 100 and 600 GeV for Ia and IIP Type SNRs.

It is expected that the effect will be similar for light cosmic ray nuclei. However details of the ionization, e.g. a high ionization potential of the Helium can result in some peculiarities of the hardening.

We expect that the effect of the hardening can be different for heavy nuclei. The matter is that the nuclei injected into DSA are single or double charged. The further ionization occurs via collisions with thermal particles (a so called stripping) and a photoionization. The photoionization is possible when accelerated particles reach high Lorentz factors and interact with optical, infrared and microwave background photons (Morlino 2011). For example, it takes  $\sim 10^5$  years for a full ionization of Iron nuclei with a Lorentz factor 100 accelerated in SNR evolving in the dense gas with a number density of  $10 \text{ cm}^{-3}$  (see Fig.1 of (Morlino 2011)). This time is higher than the age of the transition to the radiative stage  $\sim 10^4$  years. Actually the heavy nuclei have the time for the ionization up to the charge state  $\sim 10$ . They will be stripped further after the end of the acceleration and during a propagation in the Galaxy. Therefore it is expected that heavy nuclei have lower observable rigidities of the hardening.

It is important to note that high-energy measurements of protons and nuclei energy spectra in the cosmic ray experiment AMS confirm the earlier experimental results of ATIC-2, CREAM and PAMELA measurements on the presence of spectral hardening at magnetic rigidity at about 200 GV (see e.g. review of Serpico (2018) and references therein). Some peculiarities for the hardening of Iron nuclei were also reported (Schroer et al. 2021).

The nature of this hardening is not clear yet. In principle it may reflect the source spectra or the peculiarity of the energy dependence of cosmic ray leakage time from the Galaxy.

In our modeling the hardening at energies 100 – 500 GeV in the source proton and electron spectra is related with a higher acceleration efficiency after the full reionization of the medium just before the beginning of the radiative stage and with the strong gas compression behind the shock at the radiation stage. Probably this spectral feature is also presented in the energy dependence of the cosmic ray leakage time because of the self-confinement of cosmic rays (see a review of Blasi (2019) and references therein). In self-confinement models, cosmic rays generate MHD waves via cosmic ray streaming instability. These waves in turn scatter cosmic ray particles and regulate their diffusion and confinement in the Galaxy. The streaming instability is produced mainly by protons and  $\alpha$ -particles. So the hardening in their source spectra will result in a change of the energy dependence of the interstellar diffusion coefficient.

## 6 CONCLUSION

Our results and conclusions are the following:

1) We performed the modeling of particle acceleration in SNRs up to the late stages of the remnant evolution when almost all particles accelerated at the forward shock have left the remnant.

2) We show that transition to the radiative phase of supernova remnants is accompanied by a higher acceleration efficiency of cosmic rays. It leads to the hardening of the cosmic ray proton and electron source spectrum at energies of several hundreds GeV. This energy is simply the maximum energy of accelerated particles at the time of the transition. Cosmic ray particles at lower energies are mainly accelerated and escaped the remnant at the radiative stage.

3) The effect is stronger for cosmic ray electrons because of the higher electron injection rate in old SNRs.

4) We expect that the effect is different for heavy nuclei because of the partial ionization.

## ACKNOWLEDGEMENTS

The work was partially supported by the Russian Foundation for Basic Research grant 19-02-00043. The work was also partly performed at the Unique scientific installation "Astrophysical Complex of MSU-ISU" (agreement 13.UNU.21.0007). We also thank the referee Luke Drury for valuable comments.

## DATA AVAILABILITY

All results in this paper were obtained using available published data.

## REFERENCES

- Ackermann, M., Ajello, M., Allafort, A., et al. 2013, *Sci*, 339, 807  
 Archambault, S., Archer, A., Benbow W. et al. 2017, *ApJ*, 836, 23  
 Arnaud M., Ashdown M., Atrio-Barandela F. et al., 2016, *A&A* 586, 134  
 Axford, W.I., Leer, E., Skadron, G., 1977, *Proc. 15th ICRC*, Plovdiv, 90, 937  
 Badenes, C., Borkowski, K.J., Hughes, J.P., Hwang, U., & Bravo, E., 2006, *ApJ* 645,1373  
 Bell, A.R., 1978, *MNRAS*, 182, 147  
 Bell, A.R., 2004, *MNRAS*, 353, 550  
 Bell, A.R., 2014, *Astropart. Phys.*, 43, 56  
 Blandford, R.D., Ostriker, J.P. 1978, *ApJ*, 221, L29  
 Blasi, P., 2019, *Galaxies* 7, 64  
 Bykov, A.M., Malkov, M.A., Raymond, J.C., Krassilchchikov, A.M., Vladimirov, A.E., 2013, *Space Science Rev.* 178, 599  
 Caprioli, D., 2014, *Nuclear Physics B (Proc. Suppl.)*, 256, 48  
 Caprioli, D., Haggerty, C.C., Blasi, P., 2020, *ApJ*, 905, 2  
 Castelletti, G., Dubner, G., Brogan, C., & Kassim, N.E., 2007, *A&A* 471, 537  
 Chevalier R. 1999, *Astrophys. J.* 511, 798.  
 Chevalier, R., 2005, *ApJ*, 619, 839  
 Drury, L.O'C, Duffy, P., Kirk, J.G., 1996, *A&A* 309, 1002  
 Haggerty, C.C., Caprioli, D., 2020, *ApJ*, 905, 1  
 Klein, U., Emerson, D.T., Haslam, C.G.T., & Salter, C.J., 1979, *A&A*, 76, 120  
 Koo, B.-C., Heils, C., 1995, *ApJ* 442, 679  
 Krymsky, G.F. 1977, *Soviet Physics-Doklady*, 22, 327  
 Landini, M., Monsegnori Fossi, B.C., *Astron. Astrophys. Suppl.*, 1990, 82, 229  
 Lee S.H., Patnaude D.J., Raymond J.C. et al. 2015, *ApJ* 806, 71  
 Lemoine-Goumard M. *Proceedings of IAU Symposium* 2014, 296, 287  
 McKenzie, J.F., Völk, H.J., 1982, *A&A*, 116, 191

- Moffatt, H. K., 1986, *J. Fluid Mech* 166, 359.
- Morlino, G., 2011, *MNRAS* 412, 2333
- Morlino, G., Blasi, P., Bandiera, R., Amato, E., Caprioli, D., 2013, *ApJ* 768, 148
- Park, G., Koo, B.-C., Gibson, S. J. et al., 2013, *ApJ* 777, 14
- Ptuskin, V.S., Zirakashvili, V.N., Seo, E.S. 2010, *ApJ*, 718, 31
- Reach, W.T., Rho, J., Jarrett, T.H., 2005, *ApJ* 618,297
- Sarkar, K.C., Gnat, O., Sternberg, A., 2021, *MNRAS*, 504, 583
- Serpico, P.D., 2018, *J. Astrophys. Astronomy* , 39, id41
- Schroer, B., Evoli, C., Blasi, P., 2021, *Phys. Rev. D*, 103, 123010
- Tamagawa, T., Hayato, A., Nakamura, S. et al., 2009, *PASJ* 61, S167
- Zirakashvili, V.N., Ptuskin, V.S., 2008a, *ApJ*, 678, 939
- Zirakashvili V.N., Ptuskin V.S., 2008b, arXiv: 0807.2754.2008
- Zirakashvili, V.N., Ptuskin V.S. 2012, *Astropart. Phys.*, 39, 12
- Zirakashvili, V.N., Ptuskin, V.S., 2016a, *Astropart. Physics*, 78, 28
- Zirakashvili, V.N., Ptuskin, V.S., 2016b, arXiv: 1701.00844
- Zirakashvili, V.N., 2018 *Intern. J. Mod. Phys. D*, 27, 1844023-1081-8
- Zirakashvili, V.N., Ptuskin, V.S., 2018a, *Astron. Letters*, 44, 769
- Zirakashvili, V.N., Ptuskin, V.S., 2018b, *Astropart. Phys.* 98, 21
- Zirakashvili, V.N., Ptuskin, V.S., 2021, *Bulletin of the Russian Academy of Sciences* 85, 366

This paper has been typeset from a  $\text{\TeX}/\text{\LaTeX}$  file prepared by the author.